Xue et al. Nanoscale Research Letters (2018) 13:114
https://doi.org/10.1186/s11671-018-2522-5

Nanoscale Research Letters

NANO EXPRESS Open Access

S-Doped Sb_2O_3 Nanocrystal: an Efficient Visible-Light Catalyst for Organic Degradation

Hun Xue[1,3], Xinyi Lin[1], Qinghua Chen[1], Qingrong Qian[1], Suying Lin[2,3], Xiaoyan Zhang[2], Da-Peng Yang[2*] and Liren Xiao[1*]

Abstract

The S-doped Sb_2O_3 nanocrystals were successfully synthesized using $SbCl_3$ and thioacetamide (TAA) as precursors via a facile one-step hydrothermal method. The effects of pH of the precursor reaction solution on the product composition and property were determined. The results indicated that the doping amount of S could be tuned by adjusting the pH of the precursor solution. Furthermore, the S entered into the interstitial site of Sb_2O_3 crystals as S^{2-}, which broadened the absorption wavelength range of the Sb_2O_3 nanocrystal. The S-doped Sb_2O_3 exhibited an excellent visible-light-driven photocatalytic activity in the decomposition of methyl orange and 4-phenylazophenol. Last, a possible photocatalytic mechanism of the S-doped Sb_2O_3 under visible light irradiation was proposed.

Keywords: S-doped Sb_2O_3, Hydrothermal synthesis, Photocatalysis, Visible light, Organic degradation

Background

The semiconductor photocatalytic oxidation is an ideal environmental purification technique due to its utilization of solar energy, high stability, and nontoxicity. It can effectively remove organic pollutants, even at extremely low concentration, without causing any secondary pollution [1–6]. Among various kinds of semiconductor photocatalysts, TiO_2 is widely investigated due to its excellent performance under UV irradiation on mineralization of a variety of organic compounds. However, the narrow band gap of TiO_2 (3.2 eV) limits its utilization efficiency of solar energy [7, 8]. Therefore, developing the novel visible-light-driven photocatalysts is of great importance in environmental purification.

Currently, the visible-light-driven photocatalysts can be prepared via two major strategies: one is to develop new single-phase photocatalysts, such as CdS, $Sn_2Nb_2O_7$, $CaBi_2O_4$, $BiWO_4$, and $SnIn_4S_8$ [9–13], and the other one is to modify the UV-active photocatalysts. The modification can be realized by doping foreign elements, coupling UV-active photocatalysts with narrow band gap semiconductors, as well as forming inorganic-organic hybridization [14–30]. Sulfur (S), a non-metal element, is usually used to dope wide-band gap semiconductors, such as TiO_2 [18–20], $In(OH)_3$ [21], and Zn_2SnO_4 [22], to obtain the desired visible-light photocatalysts. However, the doping condition can significantly affect the valence state and form of S in the products, resulting in various photocatalytic activities. For example, Umebayashi et al. prepared the S-doped TiO_2 by the oxidation annealing of TiS_2, where the S atoms occupied the O atom sites in TiO_2 to form Ti–S bonds [18]. Ohno et al. hydrolyzed titanium alkoxide in the presence of thiourea, and the hydrolysis product was calcined in the air to afford S^{4+} and S^{6+} substituted TiO_2 [19]. Devi et al. prepared the S-doped TiO_2 by a sol-gel method using sulfur powder as the S source. They found that S^{6+} was incorporated into the Ti^{4+} lattice of the TiO_2 crystal [20]. S anion-doped Zn_2SnO_4 was prepared by calcining the mixture of thiourea and spinel Zn_2SnO_4 under argon atmosphere, during which S^{2-} ion entered into the interstitial site of Zn_2SnO_4 crystal [22].

The oxides and complex oxides of p-block metal antimony, such as Sb_2O_3 [31], $M_2Sb_2O_7$ (M=Ca and Sr) [32, 33], $NaSbO_3$ [32], $Sr_{1.36}Sb_2O_6$ [34], $ZnSb_2O_6$ [35] and $GaSbO_4$

* Correspondence: yangdp@qztc.edu.cn; xlr1966@126.com
[2]College of Chemical Engineering and Materials Sciences, Quanzhou Normal University, Quanzhou 362000, China
[1]Fujian Key Laboratory of Pollution Control & Resource Reuse, Fujian Normal University, Fuzhou 350007, China
Full list of author information is available at the end of the article

[36], have unique crystal structures and electronic structures that can promote the photogenerated charge separation and reduce the recombination of photogenerated electrons and holes and thus have attracted considerable attentions as novel photocatalytic materials. However, most of them only respond to ultraviolet light, which limits their further applications. In the present work, S^{2-}-doped Sb_2O_3 nanocrystal was prepared using $SbCl_3$ and thioacetamide (TAA) as the sulfur source by a hydrothermal synthesis method. The effects of the S doping on the visible-light-driven photocatalytic activity of Sb_2O_3 for the degradation of methyl orange (MO) and 4-phenylazophenol were also evaluated. The results indicated that the S^{2-} doping was able to effectively narrow the band gap of Sb_2O_3 and thus improved the visible-light-driven photocatalytic activity of the Sb_2O_3. Our work provided a feasible synthesis route of the visible-light-responsive S-doped Sb composite oxide photocatalysts for efficient solar energy utilization.

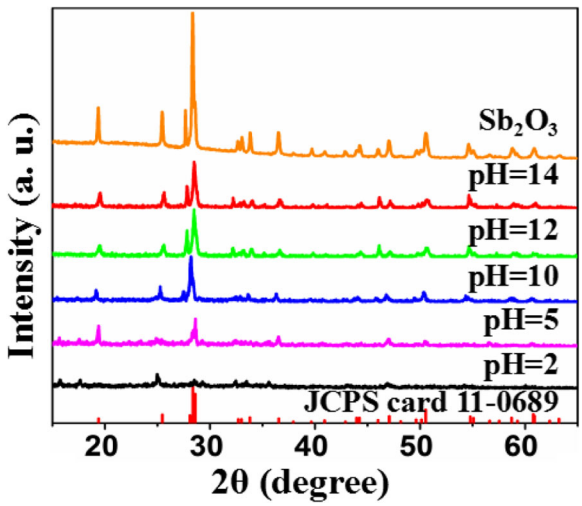

Fig. 1 XRD patterns of Sb_2O_3 and S-doped Sb_2O_3 synthesized at various pHs (pH = 2, 5, 10, 12, and 14)

Methods

Synthesis of S-Doped Sb_2O_3 Nanocrystals

All chemicals used in this work were purchased from Aladdin reagent and used directly. The S-doped Sb_2O_3 nanocrystals were synthesized by a hydrothermal method using $SbCl_3$ and thioacetamide (TAA) as the precursors. Briefly, 3 mmol $SbCl_3$ was added into a 100-mL Teflon-lined stainless steel autoclave reactor containing 70 mL deionized water and mechanically stirred for 15 min. Then, 4 mmol TAA was added into the mixed solution under constant stirring. The pH of the precursor solution was adjusted to 2, 5, 10, 12, and 14 using HCl or NaOH solution. The precursor solution was heated at 120 °C in an oven for 12 h. The produced precipitate was washed with distilled water and absolute ethanol several times and dried in the air at 70 °C. The products obtained at different pH were denoted as Sb_2O_3-S-pH (pH = 2, 5, 10, 12, and 14). The pure Sb_2O_3 was prepared in the absence of TAA using the similar procedure. Briefly, 3 mmol $SbCl_3$ was dissolved in 50 mL deionized water and 20 mL absolute ethanol in a 100-mL Teflon-lined stainless steel autoclave reactor under vigorous stirring and heated at 120 °C for 12 h. The produced precipitate was washed with distilled water and absolute ethanol for several times. The obtained products were obtained after being dried at 70 °C.

Material Characterization

The powder X-ray diffraction (XRD) patterns of the as-prepared Sb_2O_3 nanocrystals were recorded on a Bruker D8 Advance X-ray diffractometer using CuK_α radiation operated at the accelerating voltage of 40 kV and the applied current of 40 mA. The ultraviolet-visible diffuse reactance spectra (UV–vis DRS) were collected on a UV–vis spectrometer (Cary 500 Scan Spectrophotometers, Varian, USA) using $BaSO_4$ as the reflectance standard. The transmission electron microscopy (TEM) and high resolution transmission electron microscopy (HRTEM) images were captured using a JEOL model JEM 2010 EX instrument operated at the accelerating voltage of 200 kV. X-ray photoelectron spectra (XPS) were recorded on a PHI Quantum 2000 XPS System equipped with a monochromatic Al K_α source and a charge neutralizer. The sample powder was ultrasonically dispersed in ethanol, and a drop of the suspension was dropped on a carbon film coated on a 3-mm-diameter fine-mesh copper grid. The C 1s peak at 284.8 eV of the surface adventitious carbon was used as the reference for all binding energies. Raman scattering spectra were obtained using a Renishaw inVia Raman microscope at room temperature.

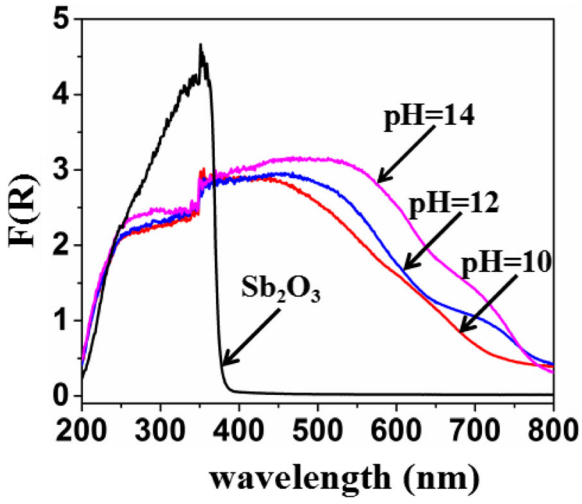

Fig. 2 Diffuse reflectance absorption spectra of Sb_2O_3 and Sb_2O_3-S-pH (pH = 10, 12, and 14)

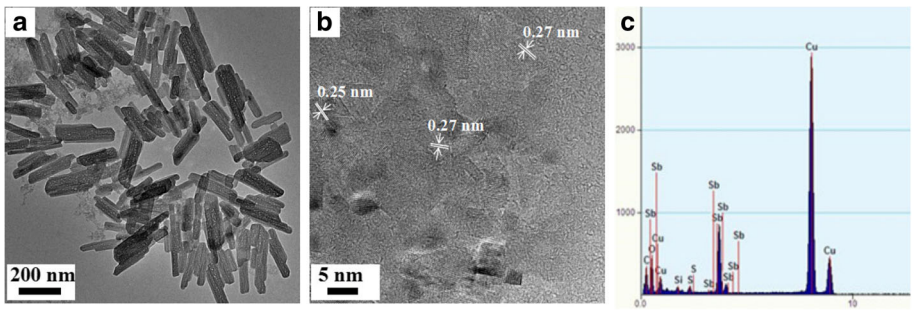

Fig. 3 **a** TEM. **b** HRTEM images and **c** EDS spectrum of Sb_2O_3-S-12

Photocatalytic Activity Measurements

The photocatalytic activity of the samples was carried out in a photoreaction vessel. A 500 W halogen lamp (Philips Electronics) was positioned beside the cylindrical reaction vessel with a plane side as the visible light source. Two cut-off filters of 420 and 800 nm were placed between the lamp and the vessel to ensure only visible light passed to reach the vessel. The vessel was maintained at room temperature by circulating water. The photocatalyst (80 mg) was powdered and added to the vessel containing 80 mL 3×10^{-5} mol L^{-1} MO or *p*-hydroxyazobenzene (1.2×10^{-4} mol L^{-1}) aqueous solution. The mixture was stirred in the dark for 1 h to reach the adsorption/desorption equilibrium on the photocatalyst and then exposed to the visible light. A 4 mL suspension was taken at certain time intervals and centrifuged. The supernatant was collected and measured with a Shimadzu UV-1750 UV–Vis–NIR spectrophotometer. The absorbance at the maximum absorption was recorded.

Results and Discussion

The XRD patterns of the control Sb_2O_3 and Sb_2O_3-S-pH (pH = 2, 5, 10, 12, and 14) are shown in Fig. 1. All peaks of both control sample and Sb_2O_3-S-pH (pH = 10, 12, and 14) were indexed to Sb_2O_3 (JCPDS card 11-0689). The low pHs (2 and 5) of the precursor solution lowered the crystallinity of the product and caused the formation of impure phases. These observations indicated that the pH of precursor solution could significantly affect the composition of the products, and the pure Sb_2O_3 phase could only be obtained under alkaline conditions. The intensities of all characteristic XRD peaks of Sb_2O_3 were higher than those of Sb_2O_3-S-pH (pH = 10, 12, and 14), indicating that TAA inhibited the growth of Sb_2O_3 crystallite.

Figure 2 shows the UV–vis diffuse reflectance spectra of Sb_2O_3 and Sb_2O_3-S-pH (pH = 10, 12, and 14). The maximum absorption of Sb_2O_3 appeared at ca. 380 nm, suggesting that Sb_2O_3 only responded to UV irradiation. Compared with that of pure Sb_2O_3, the band-gap transitions of Sb_2O_3-S-pH (pH = 10, 12, and 14) exhibited obvious redshifts, and the redshift increased with the increase of the pH of the precursor solution. Therefore, it is reasonable to believe that the band gap narrowing was dominantly attributed to the S doping. The S 3p states mixed with valence band (VB), which increased the width of VB and lowered the energy shift in the optical absorption [18]. It is well known that TAA can be hydrolyzed to generate S^{2-} in an alkaline solution and the increased pH

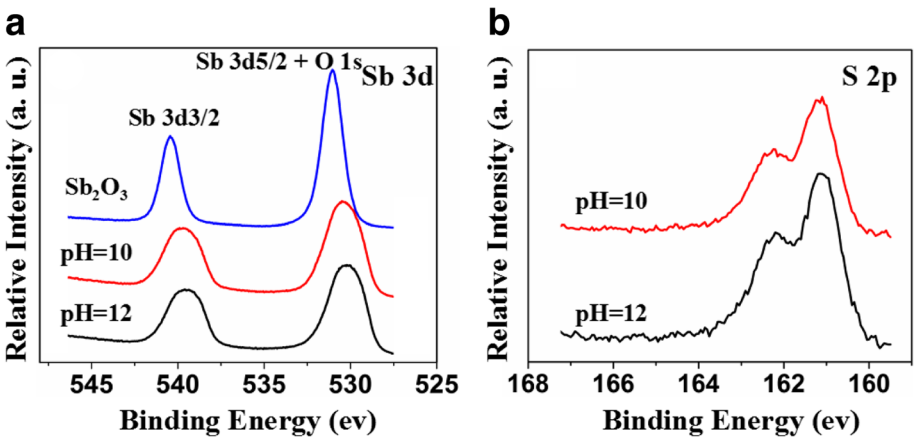

Fig. 4 XPS spectra of Sb_2O_3 and Sb_2O_3-S-pH (pH = 10 and 12). **a** Sb 3d. **b** S 2p

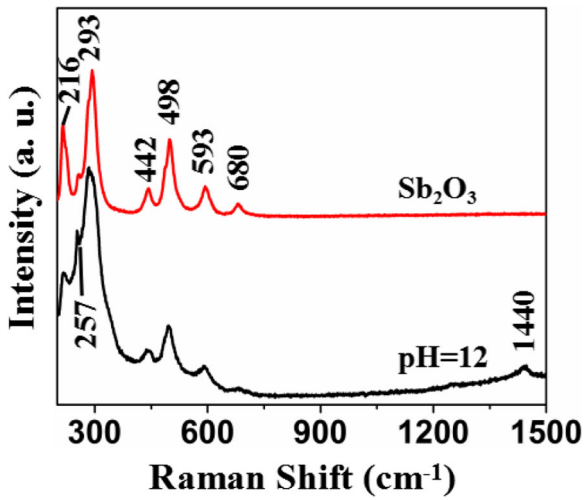

Fig. 5 Raman spectra of Sb_2O_3 and Sb_2O_3-S-12

can promote the production of S^{2-}. Therefore, the increases in the redshift of the band-gap transition with the pH of precursor solution might be attributed to the increased amounts of S doped in Sb_2O_3 at higher pHs. Therefore, the S doping amount can be controlled by simply adjusting the pH of the precursor solution.

TEM was done to identify the morphology and crystal structure of S-doped Sb_2O_3. As shown in Fig. 3a, the Sb_2O_3-S-12 was rod-shaped with a diameter of ~ 40 nm and length ranging from 100 to 200 nm. The HRTEM image revealed that the nanorods were consisted of many randomly assembled nanoparticles with an average diameter of ~ 5 nm (Fig. 3b). Clear diffraction patterns with interplanar distances of 0.25 and 0.27 nm were observed in the HRTEM images, which can be assigned to the (200) and (131) planes of Sb_2O_3, respectively. The EDS analysis (Fig. 3c) revealed that Sb, O, and S elements existed in the samples, indicating that the S-doped Sb_2O_3 was successfully prepared.

The XPS spectra and high-resolution Sb 3d and the O 1s XPS spectra of Sb_2O_3 and Sb_2O_3-S-pH (pH = 10 and 12) are displayed in Fig. 4a. The Sb 3d 3/2 peak of Sb_2O_3 appeared at 539.8 eV and the peak at 530.5 eV were assigned to Sb 3d 5/2 and O 1s, suggesting that the oxidation state of Sb is + 3 instead of + 5 with slightly higher binding energies [37, 38]. The S doping reduced the binding energies of Sb 3d, yet showed no significant effects on the chemical state of Sb. These results indicated that the S doping changed the chemical environments of the Sb ions and increased the electron densities around the Sb ions due to the lower electronegativity of S [39]. Compared with Sb_2O_3-S-10, Sb_2O_3-S-12 contained more S. The electron density around its Sb was higher than that of Sb_2O_3-S-10, and thus, the Sb 3d binding energy of Sb_2O_3-S-12 shifted towards low energy direction. The S 2p high-resolution XPS spectra in Fig. 4b revealed two peaks at 161.5 and 162.7 eV which were attributed to S^{2-} [22, 40, 41]. The radius of S^{2-} (184 pm) is much greater than that of O^{2-} (132 pm). Therefore, it was difficult for S^{2-} to replace the O^{2-} in Sb_2O_3 [22, 42]. It is most likely that S^{2-} entered into the interstitial site of the Sb_2O_3 crystal [18]. XPS analysis indicated that Sb_2O_3-S-12 contained more S than Sb_2O_3-S-10, further confirming that the pH of the precursor solution could be used to control the S doping amount.

Figure 5 shows the Raman spectra of the Sb_2O_3 and Sb_2O_3-S-12. Sb_2O_3 exhibited signal at 216, 257, 293, 442, 498, 593, and 680 cm^{-1}. A new peak appeared at 1440 cm^{-1} in the spectra of Sb_2O_3-S-12, which might be the result from the S doping. In addition, compared to the peaks of Sb_2O_3, the peak width of the peaks of Sb_2O_3-S-12 increased and the symmetry of their peak shapes decreased, indicating that the S doping increased the internal defects [43]. The S doped into the interstitial site of Sb_2O_3 crystals caused the deformation of the lattice.

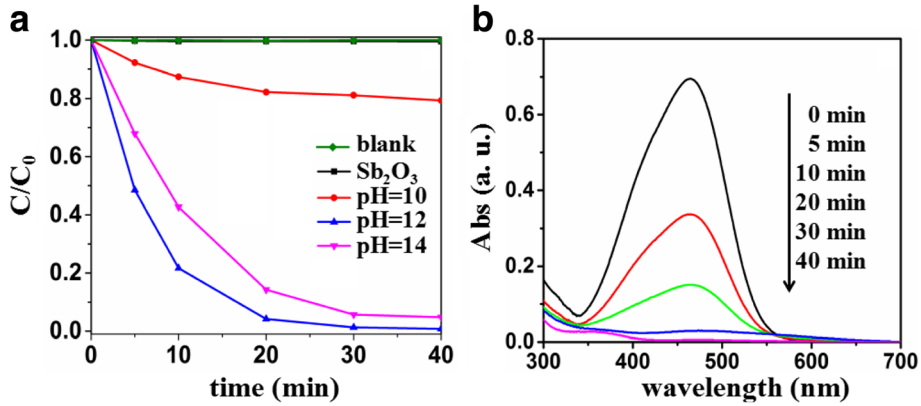

Fig. 6 a Temporal changes of MO concentration as monitored by the UV–vis absorption spectra at 464 nm on Sb_2O_3 and Sb_2O_3-S-pH (pH = 10, 12, and 14). **b** Temporal absorption spectral patterns of MO during the photodegradation process over Sb_2O_3-S-12

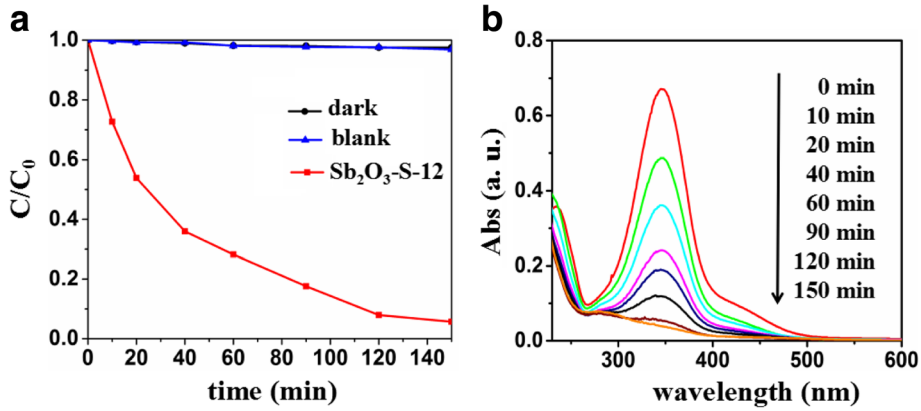

Fig. 7 **a** Temporal changes of 4-phenylazophenol concentration as monitored by the UV–vis absorption spectra at 347 nm on Sb_2O_3-S-12. **b** Temporal absorption spectral patterns of 4-phenylazophenol during the photodegradation process over Sb_2O_3-S-12

The visible-light-driven photocatalytic activities of pure and S-doped Sb_2O_3 for the degradation of MO were determined. The temporal changes in the MO concentration were monitored by measuring the UV–vis absorption of the MO solution over the photocatalyst at 464 nm (Fig. 6a). MO appears very stable under visible light with almost no degradation. Since the Sb_2O_3 could not be excited under visible light, the MO degradation was negligible in the presence of Sb_2O_3. Doping with certain amount of S would enhance the visible light absorption, increase the internal defects, and promote the separation rate of the photogenerated electron-hole pairs. As a result, the visible-light-driven photocatalytic activity of the samples could be improved, which can be demonstrated by the S-doped Sb_2O_3. It is noteworthy that the photocatalytic activities of the S-doped Sb_2O_3 prepared at different pHs were different. Sb_2O_3-S-10 exhibited the lowest visible-light-driven photocatalytic activity. It can be explained that the hydrolysis of TAA under weak alkaline conditions is weak, producing less S^{2-}. The Sb_2O_3-S-14 with more S produced under strong alkaline condition exhibit a lower photocatalytic activity compared with the Sb_2O_3-S-12 with relatively less S, which may be attributed to the excessive S doping causing too many defects that were the recombination centers of the photogenerated electron-hole pair. Compared with the counterparts, Sb_2O_3-S-12 exhibited the highest visible-light-driven photocatalytic activity and was able to degrade 99.2% MO in 40 min under visible light irradiation. Figure 6b shows the temporal absorption spectral patterns of MO during the photodegradation over Sb_2O_3-S-12. The absorption of MO was at 464 nm, which was attributed to its –N=N– unit. The absorption intensity decreased as the visible light irradiation proceeded, indicating that the –N=N– double bonds were gradually decomposed [44].

The photocatalytic performance of Sb_2O_3-S-12 for the degradation of p-hydroxyazobenzene was also determined. Figure 7a, b presents the photocatalytic activity of Sb_2O_3-S-12 for the p-hydroxybenzobenzene degradation and the corresponding UV–vis absorption spectra of p-hydroxybenzobenzene during the degradation. No

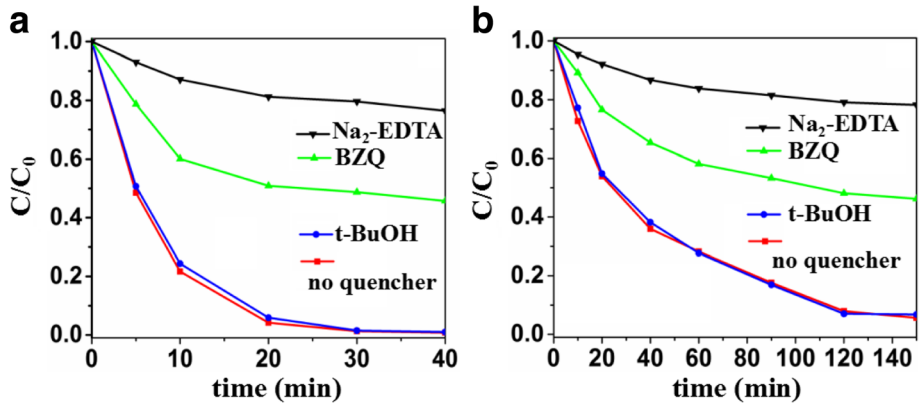

Fig. 8 Trapping experiment of active species over Sb_2O_3-S-12 during the photocatalytic degradation of **a** MO. **b** 4-Phenylazophenol

p-hydroxyazobenzene degradation was observed under the visible light irradiation in the absence of Sb_2O_3-S-12. In contrast, 94.3% of p-hydroxyazobenzene was degraded under the visible light irradiation for 150 min in the presence of Sb_2O_3-S-12. In addition, the absorption of p-hydroxybenzobenzene at 347 nm decreased as the irradiation prolonged. These results indicated that S-doped Sb_2O_3 could be implemented in the degradations of different pollutants.

To explore the photocatalytic mechanism of the S-doped Sb_2O_3 nanocrystals, the major oxidative species in the photocatalytic reaction were trapped using *p*-benzoquinone (BZQ, an O_2^-· radical scavenger), disodium ethylene diamine tetra acetate (Na_2-EDTA, a hole scavenger), and tert-butanol (t-BuOH, a OH· radical scavenger) [39, 45]. As shown in Fig. 8, the addition of t-BuOH showed no deleterious effect on the photocatalytic activity of Sb_2O_3-S-12 and the presence of BZQ or Na_2-EDTA decelerated significantly its photocatalytic degradation efficiency of MO and 4-phenylazophenol. Therefore, it can be concluded that h^+ and O_2^-· radicals were the dominant oxidative species of the S-doped Sb_2O_3 photocatalysis and the OH· radical was not involved.

Based on these discussions, a possible mechanism for photocatalytic degradation of MO over S-doped Sb_2O_3 nanocrystals was proposed as follows (Scheme 1). S-doped Sb_2O_3 can be efficiently excited to create holes in VB and electrons in conduction band (CB) under visible light irradiation. The S doping increased the VB width of Sb_2O_3. The electrons are long-lived enough to react with adsorbed O_2 to produce O_2^-· radicals. The photogenerated h^+ and O_2^-· exhibited a strong oxidation potential which can directly oxidize MO and 4-phenylazophenol to degradated products.

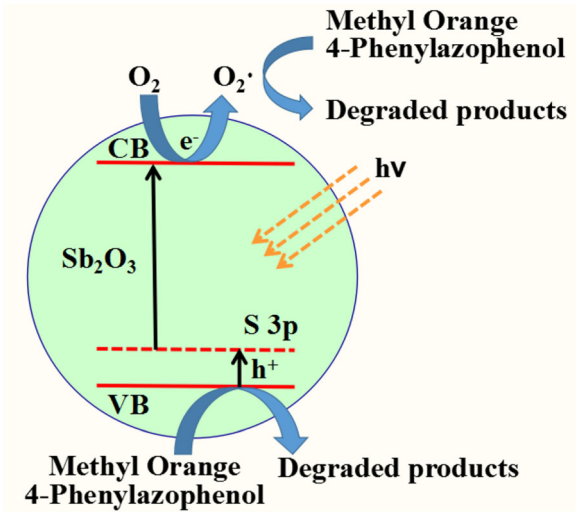

Scheme 1 Possible mechanism of the photocatalytic degradation of MO or 4-phenylazophenol over Sb_2O_3-S-12 visible-light photocatalyst

Conclusions

The S-doped Sb_2O_3 nanocrystals were successfully prepared from $SbCl_3$ and TAA via a facile one-step hydrothermal method under alkaline conditions. S entered into the interstitial site of Sb_2O_3 crystals as S^{2-}, which broadened its visible light absorption range. The pH of the precursor solution can significantly affect the S doping amount, which further alternates the visible-light-driven photocatalytic activity of the S-doped Sb_2O_3 nanocrystal. The nanocrystal prepared at pH 12 exhibited the highest visible-light-driven photocatalytic activity and was able to degrade 99.2% MO and 94.3% p-hydroxybenzobenzene in 40 and 150 min, respectively, under visible light irradiation. The visible-light photocatalytic degradation of MO and *p*-hydroxyazobenzene by S-doped Sb_2O_3 were achieved by h^+ and O_2^-·.

Abbreviations

BZQ: *p*-Benzoquinone; MO: Methyl orange; Na_2-EDTA: Disodium ethylene diamine tetra acetate; S: Sulfur; TAA: Thioacetamide; t-BuOH: Tert-butanol

Funding

This work was supported by the National Natural Science Foundation of China (21307012, 81472001, 31400851, 21536010) and Educational Commission of Fujian Province (JK2013007, 2014J01035, JA15138).

Availability of Data and Materials

We declared that the materials described in the manuscript, including all relevant raw data, will be freely available to any scientist wishing to use them for non-commercial purposes, without breaching participant confidentiality.

Authors' Contributions

HX, QHC, QRQ, SYL, XYZ, DPY, and LRX conceived and designed the experiments. HX and XYL performed the experiments. HX and DPY wrote the paper. All authors discussed the results and commented on the manuscript. All authors read and approved the final manuscript.

Competing Interests

The authors declare that they have no competing interests.

Publisher's Note

Author details

[1]Fujian Key Laboratory of Pollution Control & Resource Reuse, Fujian Normal University, Fuzhou 350007, China. [2]College of Chemical Engineering and Materials Sciences, Quanzhou Normal University, Quanzhou 362000, China. [3]Fujian Provincial Key Laboratory of Ecology-toxicological Effects & Control for Emerging Contaminants, Putian University, Putian 351100, China.

Received: 2 February 2018 Accepted: 9 April 2018
Published online: 23 April 2018

References

1. Zhao J, Yang XD (2003) Photocatalytic oxidation for indoor air purification: a literature review. Build Environ 38:645–654
2. Gao P, Liu JC, Sun DD, Ng W (2013) Graphene oxide-CdS composite with high photocatalytic degradation and disinfection activities under visible light irradiation. J Hazard Mater 250-251:412–420
3. Chan JYT, Ang SY, Ye EY, Sullivan M, Zhang J, Lin M (2015) Heterogeneous photo-Fenton reaction on hematite (α-Fe_2O_3){104}, {113} and {001} surface facets. Phys Chem Chem Phys 17:25333–25341
4. Ye EY, Zhang SY, Lim SH, Bosman M, Zhang ZH, Win KY et al (2011) Ternary cobalt-iron phosphide nanocrystals with controlled compositions, properties,

and morphologies from nanorods and nanorice to split nanostructures. Chem Eur J 17:5982–5988
5. Tee SY, Ye EY, Pan PH, Lee CJJ, Hui HK, Zhang SY et al (2015) Fabrication of bimetallic Cu/Au nanotubes and their sensitive, selective, reproducible and reusable electrochemical sensing of glucose. Nano 7:11190–11198
6. Liu SH, Gao HT, Ye EY, Low M, Lim SH, Zhang SY et al (2010) Graphitically encapsulated cobalt nanocrystal assemblies. Chem Commun 46:4749–4751
7. Daghrir R, Drogui P, Robert D (2013) Modified TiO_2 for environmental photocatalytic applications: a review. Ind Eng Chem Res 52:3581–3599
8. Ren HJ, Koshy P, Cao FY, Sorrell CC (2016) Multivalence charge transfer in doped and co doped photocatalytic TiO_2. Inorg Chem 55:8071–8081
9. Karunakaran C, Senthilvelan S (2005) Solar photocatalysis: oxidation of aniline on CdS. Sol Energy 79:505–512
10. Zhou C, Zhao YF, Bian T, Shang L, Yu HJ, Wu LZ et al (2013) Bubble template synthesis of $Sn_2Nb_2O_7$ hollow spheres for enhanced visible-light-driven photocatalytic hydrogen production. ChemInform 44:9872–9874
11. Tang JW, Zou ZG, Ye JH (2004) Efficient photocatalytic decomposition of organic contaminants over $CaBi_2O_4$ under visible-light irradiation. Angew Chem Int Edit 43:4463–4466
12. Fu HB, Pan CS, Yao WQ, Zhu YF (2005) Visible-light-induced degradation of rhodamine B by nanosized Bi_2WO_6. Phys Chem B 109:22432–22439
13. Yan TJ, Li LP, Li GS, Wang YJ, Hu WB, Guan XF (2011) Porous $SnIn_4S_8$ microspheres in a new polymorph that promotes dyes degradation under visible light irradiation. J Hazard Mater 186:272–279
14. Kong LN, Wang CH, Zheng H, Zhang XT, Liu YC (2015) Defect-induced yellow color in Nb-doped TiO_2 and its impact on visible-light photocatalysis. J Phys Chem C 119:16623–16632
15. Xu JH, Wang WZ, Sun SM, Wang L (2012) Enhancing visible-light-induced photocatalytic activity by coupling with wide-band-gap semiconductor: a case study on Bi_2WO_6/TiO_2. Appl Catal B Environ 111:126–132
16. Liao GZ, Chen S, Quan X, Chen H, Zhang YB (2010) Photonic crystal coupled TiO_2/polymer hybrid for efficient photocatalysis under visible light irradiation. Environ Sci Technol 44:3481–3485
17. Shamaila S, Sajjad AKL, Chen F, Zhang JL (2011) WO_3/BiOCl, a novel heterojunction as visible light photocatalyst. J Colloid Interf Sci 356:465–472
18. Umebayashi T, Yamaki T, Itoh H, Asai K (2002) Band gap narrowing of titanium dioxide by sulfur doping. Appl Phys Lett 81:454–456
19. Ohno T, Mitsui T, Matsumura M (2003) Photocatalytic activity of S-doped TiO_2 photocatalyst under visible light. Chem Lett 32:364–365
20. Devi LG, Kavitha R (2014) Enhanced photocatalytic activity of sulfur doped TiO_2 for the decomposition of phenol: a new insight into the bulk and surface modification. Mater Chem Phys 143:1300–1308
21. Li ZH, Dong TT, Zhang YF, Wu L, Li JQ, Wang XX et al (2007) Studies on $In(OH)_yS_z$ solid solutions: syntheses, characterizations, electronic structure, and visible-light-driven photocatalytic activities. J Phys Chem C 111:4727–4733
22. Lin YX, Lin S, Luo MH, Liu JH (2009) Enhanced visible light photocatalytic activity of Zn_2SnO_4 via sulfur anion-doping. Mater Lett 63:1169–1171
23. Dou QQ, Guo HC, Ye EY (2014) Near-infrared upconversion nanoparticles for bio-applications. Mater Sci Eng C 45:635–643
24. Ye EY, Tan H, Li SP, Fan WY (2006) Self-organization of spherical, core–shell palladium aggregates by laser-induced and thermal decomposition of [Pd(PPh3)4]. Angew Chem 118:1138–1141
25. Zhang SY, Ye EY, Liu SH, Lim SH, Tee SY, Dong ZL et al (2012) Temperature and chemical bonding-directed self-assembly of cobalt phosphide nanowires in reaction solutions into vertical and horizontal alignments. Adv Mater 24:4369–4375
26. Ye EY, Zhang SY, Lim SH, Liu SH, Han MY (2010) Morphological tuning, self-assembly and optical properties of indium oxide nanocrystals. Phys Chem Chem Phys 12:11923–11929
27. Xu HT, Zheng NW, Xu HH, Wu YG, Yang RY, Ye EY et al (2002) Mn(II) ion centers in novel coordination environment: a new two-dimensional coordination polymer [Mn(3,5-pdc)·2H2O]. J Mol Struct 610:47–52
28. Tee SY, Teng CP, Ye EY (2017) Metal nanostructures for non-enzymatic glucose sensing. Mater Sci Eng C 70:1018–1030
29. Yang DP, Liu X, Teng CP, Owh C, Win KY, Lin M et al (2017) Unexpected formation of gold nanoflowers by a green synthesis method as agents for a safe and effective photothermal therapy. Nano 9:15753–15759
30. Zheng CH, Teng CP, Yang DP, Lin M, Win KY, Li ZB et al (2017) Fabrication of luminescent TiO_2:Eu^{3+} and ZrO_2:Tb^{3+} encapsulated PLGA microparticles for bioimaging application with enhanced biocompatibility. Mater Sci Eng C. https://doi.org/10.1016/j.msec.2017.10.005
31. Zhu LJ, Xue H, Xiao LR, Chen QH (2012) Preparation and photocatalytic performance of cubic Sb_2O_3 nanocrystalline. Chinese J Inorg Chem 28: 2165–2169
32. Sato J, Saito N, Nishiyama H, Inoue Y (2002) Photocatalytic water decomposition by RuO_2-loaded antimonates, $M_2Sb_2O_7$ (M=Ca, Sr), $CaSb_2O_6$ and $NaSbO_3$, with d^{10} configuration. J Photoch Photobi A 148:85–89
33. Xue H, Li ZH, Dong H, Wu L, Wang XX, Fu XZ (2008) 3D hierarchical architectures of $Sr_2Sb_2O_7$: hydrothermal syntheses, formation mechanisms, and application in aqueous-phase photocatalysis. Cryst Growth Des 8:4469–4475
34. Xue H, Chen YY, Ding N, Chen QH, Luo YJ, Liu XP et al (2016) Hydrothermal synthesis of $Sr_{1.36}Sb_2O_6$ nano-octahedrons with photocatalytic activity for overall splitting of water. Catal Commun 74:5–9
35. Liu WJ, Lin PY, Jin H, Xue H, Zhang YF, Li ZH (2011) Nanocrystalline $ZnSb_2O_6$:hydrothermal synthesis, electronic structure and photocatalytic activity. J Mol Catal A Chem 349:80–85
36. Fu YH, Xue H, Qin M, Liu P, Fu XZ, Li ZH (2012) Nanocrystalline $GaSbO_4$ with high surface area prepared via a facile hydrothermal method and its photocatalytic activity study. J Alloys Compd 522:144–148
37. Liu DN, He GH, Zhu L, Zhou WY, Xu YH (2012) Enhancement of photocatalytic activity of TiO_2 nanoparticles by coupling Sb_2O_3. Appl Surf Sci 258:8055–8060
38. He GH, Liang CJ, Ou YD, Liu DN, Fang YP, Xu YH (2013) Preparation of novel Sb_2O_3/WO_3 photocatalysts and their activities under visible light irradiation. Mater Res Bull 48:2244–2249
39. Guo MN, Wang Y, He QL, Wang WJ, Wang WM, Fu ZY et al (2015) Enhanced photocatalytic activity of S-doped $BiVO_4$ photocatalysts. RSC Adv 5:58633–58639
40. Grigas J, Talik E, Lazauskas V (2003) Splitting of the XPS in ferroelectric SbSI crystals. Ferroelectrics 284:147–160
41. Zhou WJ, Leng YH, Hou DM, Li HD, Li LG, Li GQ et al (2014) Phase transformation and enhanced photocatalytic activity of S-doped Ag_2O/TiO_2 heterostructured nanobelts. Nano 6:4698–4704
42. Asahi R, Morikawa T, Ohwaki T, Aoki K, Taga Y (2001) Visible-light photocatalysis in nitrogen-doped titanium oxides. Science 293:269–271
43. Arcibarorozco J, Bandosz T (2015) Visible light enhanced removal of a sulfur mustard gas surrogate from a vapor phase on novel hydrous ferric oxide/graphite oxide composites. J Mater Chem A 3:220–231
44. Zhang ZH, Xu Y, Ma XP, Li FY, Liu DN, Chen ZL et al (2012) Microwave degradation of methyl orange dye in aqueous solution in the presence of nano-TiO_2-supported activated carbon (supported-TiO_2/AC/MW). J Hazard Mater 209:271–277
45. Yang XF, Cui HY, Li Y, Qin JL, Zhang RX, Tang H (2013) Fabrication of Ag_3PO_4-graphene composites with highly efficient and stable visible light photocatalytic performance. ACS Catal 3:363–369